Research Square

Preprints are preliminary reports that have not undergone peer review.
They should not be considered conclusive, used to inform clinical practice,
or referenced by the media as validated information.

Crystallographic Control of the Initial Electrochemical Reduction of Hematite

Shinie S. Awulachew
University of Duisburg-Essen
Kai S. Exner
kai.exner@uni-due.de
University of Duisburg-Essen

Article

Keywords:

Posted Date: October 30th, 2026

DOI: https://doi.org/10.21203/rs.3.rs-11322227/v1

License: This work is licensed under a Creative Commons Attribution 4.0 International License.
Read Full License

Additional Declarations: No competing interests reported.

Crystallographic Control of the Initial Electrochemical Reduction of Hematite

Shinie S. Awulachew[1], Kai S. Exner[1,2,3*]

[1] *University of Duisburg-Essen, Faculty of Chemistry, Theoretical Catalysis and Electrochemistry, Universitätsstraße 5, 45141 Essen, Germany*

[2] *Cluster of Excellence RESOLV, 44801 Bochum, Germany*

[3] *Center for Nanointegration (CENIDE) Duisburg-Essen, 47057 Duisburg, Germany*

* Corresponding author: kai.exner@uni-due.de ORCID: 0000-0003-2934-6075

Abstract

Electrochemical reduction of iron oxides enables low-temperature, sustainable iron production, yet how crystallographic orientation affects the initial reduction of hematite remains unclear. Here, we combine density functional theory + U calculations and *ab initio* molecular dynamics to study the initial electrochemical reduction of the (0001), $(10\bar{1}0)$, and $(1\bar{2}10)$ facets of α-Fe_2O_3 at different hydrogen coverages. The potential-dependent descriptor $G_{max}(U)$ reveals a pronounced crystallographic dependence: the (0001) facet consistently exhibits the lowest limiting free-energy span and thus the highest thermodynamic reduction propensity. High hydrogen coverage, the thermodynamically preferred surface state under cathodic conditions, leaves (0001) and $(10\bar{1}0)$ essentially unaffected but strongly suppresses the reduction of $(1\bar{2}10)$, revealing facet-dependent surface passivation. Upon reduction, a more metallic, Fe-rich surface forms, and the O p-band center shifts most strongly on (0001). The predicted preference for (0001) agrees with experiments on the hydrogen reduction of hematite single crystals, pointing to an intrinsic facet dependence of reducibility. Our results identify crystallographic orientation and interfacial hydrogenation as key factors in the initial electrochemical reduction of hematite and provide atomistic guidelines for controlling electrochemical iron extraction.

Introduction

Conventional iron oxide reduction is primarily carried out via the blast furnace process, which employs hydrocarbons as both the main heat source and reducing agent.[1,2] This carbon-intensive approach accounts for approximately 91% of global steel production.[1,3] In recent decades, alternative methods have emerged, with direct reduction using natural gas being one of the most prominent. While this method produces lower carbon emissions compared to blast furnaces, it still depends on fossil fuels. To further reduce emissions, recent academic and industrial efforts have increasingly focused on hydrogen- and ammonia-mediated direct reduction process.[4–11] When hydrogen is produced from renewable energy sources, this approach has the potential to eliminate CO_2 emissions from the reduction step. However, hydrogen-based reduction remains energy-intensive, requiring high operating temperatures.[12]

Electrochemical reduction of iron oxides presents a promising pathway to decarbonize iron production, offering an alternative to the hydrocarbon-dependent reduction methods currently in use.[1] Although this approach has been investigated at high temperatures using molten oxide electrolysis [13,14] and at low temperatures in aqueous systems [15,16], the latter method stands out for its advantages in operational simplicity and energy efficiency.[17,18] Low-temperature electrochemical reduction typically involves electrolytic deposition, where an iron oxide suspension is reduced to metallic iron via electrodeposition within an electrochemical cell, enabling direct recovery of solid iron from the electrode surface. This reduced iron can be used as a solid metal fuel and further processed or cast into steel.

Although the electrodeposition of iron oxides can be carried out using either acidic[19,20] or alkaline electrolytes [15,21], recent studies on systems containing iron oxide suspensions have shown that alkaline conditions lead to higher current efficiency and reduce energy consumption by approximately 30% compared to acidic media.[18] Nevertheless, the inherently low solubility of iron oxides in both acidic and alkaline environments remains a major limitation, as it restricts the availability of Fe^{2+}/Fe^{3+} ions required for electrodeposition, thereby slowing down deposition kinetics.[22–24] To overcome this challenge, activation strategies that enhance the interfacial interaction between the electrical conductor, the electrolyte, and the iron oxide have been developed. These strategies facilitate the reduction of the poorly conductive Fe_2O_3 phase, improving overall electrochemical performance.[18,25,26]

Two primary reduction mechanisms for iron oxide suspensions are currently recognized in the literature: the dissolution-deposition mechanism and the direct electron transfer mechanism, also known as the solid-state pathway.[15,21,25,27] The latter involves the adsorption of iron oxide particles onto the working electrode surface via electrostatic interactions, followed by their direct reduction to metallic iron.[25] While the coexistence of both mechanisms has been proposed[21,25], their individual contributions to the overall reduction process remains incompletely understood. Recent experimental studies suggest that the solid-state mechanism dominates over dissolution-deposition pathway. [28]

Hematite exposes crystallographically distinct surfaces characterized by different atomic coordination and Fe–O bonding environments, which may give rise to pronounced differences in their intrinsic reducibility. Experimental studies of hydrogen-based hematite reduction indeed reveal orientation-dependent reduction behavior [9,29], indicating that crystallographic anisotropy can influence the transformation kinetics. However, whether such facet-dependent trends persist under electrochemical conditions, where proton-coupled electron transfer and surface hydrogenation govern the initial reduction chemistry, remains largely unexplored.

In this study, we investigate the initial electrochemical reduction of the (0001), $(10\bar{1}0)$, and $(1\bar{2}10)$ facets of hematite (α-Fe_2O_3) via the solid-state pathway using density functional theory + U (DFT + U). Clean and hydrogenated surface states with different coverages are considered to account for the evolving interfacial chemistry under cathodic conditions. The potential-dependent $G_{max}(U)$ descriptor, based on the energetic span model [30], is employed to quantify the thermodynamic reduction propensity of the different facets and surface states. Electronic-structure analyses, including the Fe d-band and O p-band centers and the density of states, are used to characterize the accompanying changes in electronic structure. In addition, *ab initio* molecular dynamics simulations (AIMD) in explicit water are performed to assess the dynamic stability of representative surface configurations, while Fe^{2+}/Fe^{3+} deposition on the reduced surfaces is evaluated to probe the competing dissolution–deposition pathway. Our calculations reveal a pronounced crystallographic dependence of the initial reduction, with the (0001) facet consistently exhibiting the highest thermodynamic reduction propensity, in agreement with experimentally observed orientation-dependent hematite reduction.

Results

Surface models and hydrogenation states

All calculations were performed using spin-polarized DFT + U with implicit solvation; computational details are given in the **Methods** section and in Section **S1** of the SI. Stoichiometric α-Fe_2O_3 slabs exposing the three low-index facets (0001), $(10\bar{1}0)$, and $(1\bar{2}10)$ were modeled using (2 × 2) surface supercells, as shown **Figure 1a–c**, respectively. The bulk magnetic ordering, characterized by ferromagnetic alignment within individual Fe layers and antiferromagnetic coupling between adjacent Fe layers, was retained throughout all slab models. The magnetic moments in the inner slab layers remain close to the bulk values, whereas the surface Fe atoms exhibit moderately reduced moments due to their lower coordination.

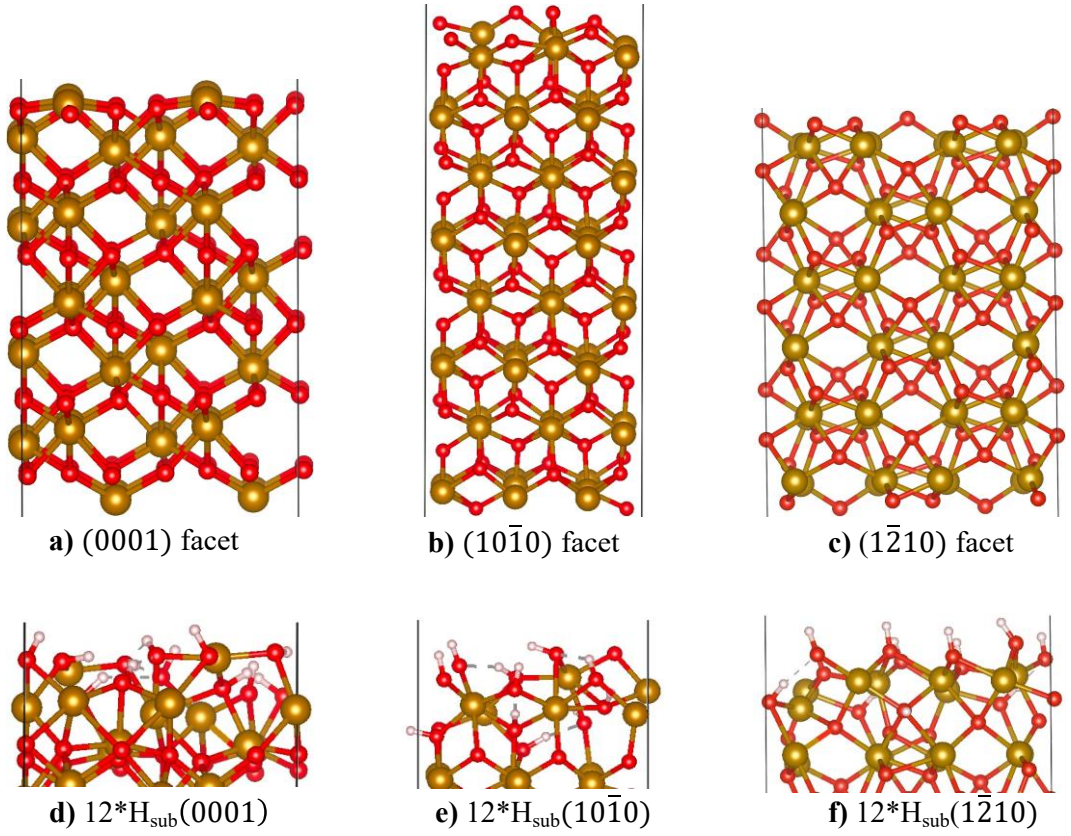


Figure 1. Slab models of the (2×2) supercell for the three low-index surfaces of α-Fe_2O_3. **a)** Side view of α-$Fe_2O_3(0001)$, **b)** side view of α-$Fe_2O_3(10\bar{1}0)$, **c)** side view of α-$Fe_2O_3(1\bar{2}10)$, **d)** side view of α-$Fe_2O_3(0001)$-12*H_{sub}, **e)** side view of α-$Fe_2O_3(10\bar{1}0)$-12*H_{sub} , and **f)** side view of α-$Fe_2O_3(1\bar{2}10)$-12*H_{sub}. Color code: gold (Fe), red (O), and white (H). While panels **a) – c)** show the full slab model used in the DFT calculations, we sketch the uppermost layers for the hydrogenated surfaces in panels **d) – f)**.

On the (0001), $(10\bar{1}0)$, and $(1\bar{2}10)$ facets of the (2 × 2) supercell, the first Fe layer contains four, six, and eight outermost iron atoms, respectively, as shown in **Figure 1**.

Computational stability diagrams (surface Pourbaix diagrams) and DFT-based surface models are widely used to assess the aqueous stability of solids and to identify surface configurations that are subsequently used for the modeling of reaction mechanisms under operating conditions.[31–34] Under cathodic conditions for electrochemical reduction of hematite, we perform hydrogenation of the three low-index facets up to a maximum coverage of 12*H_{sub} (cf. **Figure 1d-f**). The subscript "sub" denotes that hydrogen is adsorbed onto lattice oxygen atoms at the hematite surface (i.e., forming surface hydroxyl-like species). Note that hydrogenation is preferred at the oxygen surface atoms rather than the surface Fe sites, with relative free-energy differences of 1.21, 0.51, and 0.81 eV/atom for the $(0001), (10\bar{1}0)$, and $(1\bar{2}10)$ facets, respectively. The Gibbs free energies of the hydrogenated surface configurations are calculated relative to the corresponding clean surfaces in our model and are reported in **Table S1** (cf. Section **S2.3** of the Supporting Information (SI)). Based on these free energies, surface stability diagrams for the $(0001), (10\bar{1}0)$, and $(1\bar{2}10)$ facets are constructed and presented in Section **S2.4** of the SI. Although 12*H_{sub} corresponds to the thermodynamically preferred coverage under the considered conditions, the clean (cf. **Figure 1a-c**), 8*H_{sub} (cf. **Figures S2b**, **S3b**, and **S4b** for the $(0001), (10\bar{1}0)$, and $(1\bar{2}10)$ facets, respectively in Section **S2-S4** in the SI), and 12*H_{sub} surfaces (cf. **Figure 1d-f**) were selected as representative states spanning low, intermediate, and high degrees of hydrogenation. This allows the influence of progressive surface hydrogenation on the initial reduction thermodynamics to be assessed systematically. Top and side views of these three surface structures, along with their corresponding stability diagrams, are provided in **Figures S2 – S4** (cf. Section **S2.4** of the SI).

To assess the finite-temperature stability of representative surface states, AIMD simulations in explicit water were performed for the clean and 12*H_{sub}-covered hematite(0001) surfaces. During the simulation of the nominally clean surface, four water molecules spontaneously dissociated, resulting in hydroxylation of surface Fe sites and hydrogenation of lattice oxygen atoms, as shown in **Figure S49** (cf. Section **S12** of the SI). This observation indicates that the clean surface is prone to partial hydroxylation or hydrogenation under the simulated aqueous conditions. This behavior was also observed in static DFT calculations under water adsorption on the clean surfaces of hematite. [35] In contrast, the 12*H_{sub} configuration remained structurally stable throughout 20 ps trajectory without desorption or irreversible surface reconstruction. Analysis of structural metrics, including root mean-square deviation (RMSD), Fe–O coordination, bond distances, and layer-resolved atomic positions, further supports the stability of the hydrogenated surface, as further discussed in Section **S11** of the SI (**Figures S34–S48**).

The AIMD simulations therefore support the propensity of hematite surfaces toward hydroxylation and hydrogenation in an aqueous environment and the physical plausibility of hydrogenated surface states (cf. Section **S2.4** of the SI) considered in the subsequent analysis. Snapshots from the AIMD simulations at 5ps intervals are provided in **Figures S49–50** of the SI (cf. Section **S12** of the SI).

Reduction sequences and $G_{max}(U)$ analysis

The initial electrochemical reduction of hematite proceeds through successive proton-coupled electron transfer steps that progressively remove surface oxygen-containing species (*O or *OH) via water formation and generate Fe-rich reduced surface. To map the thermodynamically preferred reduction sequence under cathodic conditions, multiple surface configurations are sampled at each reduction stage and the lowest-energy structure among the configurations considered is selected as the corresponding reaction intermediate. The resulting intermediates are used to construct potential-dependent free-energy diagrams within the computational hydrogen electrode (CHE) framework. [36] A representative reduction sequence for α-Fe_2O_3(0001) clean surface is shown in **Figure 2**. The same sampling protocol is applied consistently to the (0001), $(10\bar{1}0)$, and $(1\bar{2}10)$ facets of clean and hydrogenated surfaces.

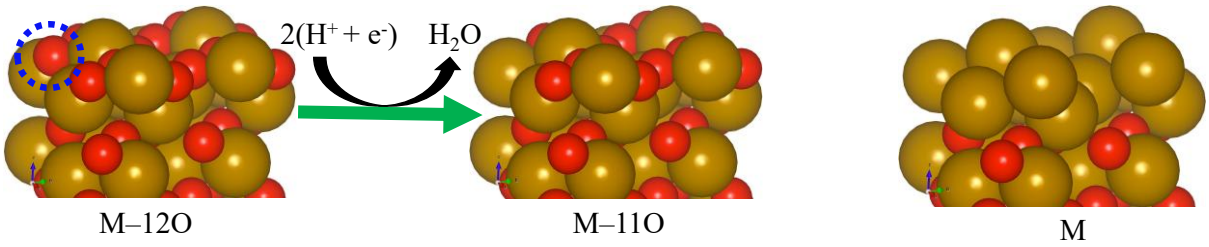


Figure 2. Elementary steps in the electrochemical reduction of hematite on the α-Fe_2O_3(0001)-clean surface. The two proton-coupled electron transfer steps and the water formation are repeated until all twelve oxygen atoms of the reactive layer(s) have been removed. Green arrows indicate the sequential reaction steps. The blue-circled site represents the preferred *O site for water formation as a byproduct, leaving behind a vacancy on the surface. The same approach holds if the reduction starts from a hydrogenated surface. Atom color code: gold (Fe), and red (O).

For the clean hematite surface, the initial reduction is modeled by the sequential removal of lattice oxygen atoms from the near-surface region. In this model, the considered surface region contains 12 oxygen atoms associated with the outermost Fe layers. Each oxygen-removal step proceeds through the transfer of two proton–electron pairs and the formation of one water molecule, generating an oxygen vacancy, as shown in **Figure 2**, according to

$$M{-}nO + 2(H^+ + e^-) \rightarrow M{-}(n{-}1)O + H_2O_{(l)} \qquad \Delta G_i \qquad (1)$$

with n = 12, 11, …, 1 and i = 1, 2, ..., 12.

Accordingly, the surface evolves sequentially along

$$M{-}12O \rightarrow M{-}11O \rightarrow M{-}10O \rightarrow \ldots \rightarrow M{-}2O \rightarrow M{-}1O \rightarrow M \qquad (2)$$

with an individual free-energy change, ΔG_i, associated with each reduction step, corresponding to complete reduction on the reactive layer(s). Here, M denotes the remaining slab after removal of the respective number of oxygen atoms from the near-surface region and does not represent a stoichiometric quantity. Thus, M−11O corresponds to a surface from which one oxygen atom has been removed relative to the initial configuration, M−10O to a surface from which two oxygen atoms have been removed, and so forth (cf. **Figure S1** of the SI). During the reduction, oxygen atoms from lower layers migrate into the outermost layers, as visible in the final structure shown in the inset of **Figure 3**, so that the reduced surfaces are not simply Fe-terminated.

The individual reaction steps associated with ΔG_1 to ΔG_{12} are provided in the SI (cf. Section **S3** of the SI), and corresponding free-energy changes are given in **Tables S2**–**S4** of the SI (cf. Section **S4** of the SI) for the (0001), $(10\bar{1}0)$, and $(1\bar{2}10)$ facets, respectively. The zero point energy (ZPE) corrections, entropy contributions, and the enthalpic contributions of the reference molecules H_2 and H_2O are provided in **Table S13** of the SI (cf. Section **S9** of the SI).

For the hydrogenated hematite surfaces, the initial reduction proceeds through the sequential removal of surface hydroxyl species. Each hydroxyl-removal step involves the transfer of one proton–electron pair and the formation of one water molecule according to

$$M{-}nOH + (H^+ + e^-) \rightarrow M{-}(n{-}1)OH + H_2O_{(l)}. \qquad \Delta G_j \qquad (3)$$

For the 8^*H_{sub} surface, the reduction sequence is

$$M{-}8OH\text{-}4O \rightarrow M{-}7OH\text{-}4O \rightarrow M{-}6OH\text{-}4O \rightarrow \ldots \rightarrow M{-}4O, \qquad (4)$$

whereas the 12^*H_{sub} surface follows

$$M{-}12OH \rightarrow M{-}11OH \rightarrow M{-}10OH \rightarrow \ldots \rightarrow M{-}1OH \rightarrow M \qquad (5)$$

with n = 8, 7, …, 1 for 8^*H_{sub}, corresponding to partial reduction, and n = 12, 11, …, 1 for 12^*H_{sub}, corresponding to complete reduction on the reactive layer(s), and j = 13, 14, ..., 32 (cf. Section **S3** of the SI). Here, M−(n−1)OH denotes the corresponding surface after removal

of one additional hydroxyl species. Thus, M−7OH-4O and M−11OH represent the first hydroxyl-vacancy states formed from the 8*H_{sub} and 12*H_{sub} surfaces, respectively.

The individual reaction steps associated with ΔG_{13} to ΔG_{32} are provided in the SI (cf. Section **S3** of the SI), and corresponding free-energy changes are given in **Tables S2**–**S4** of the SI (cf. Section **S4** of the SI) for all facets.

Potential-dependent free-energy diagrams are constructed using the CHE approach [36] for the reduction pathways of the α-$Fe_2O_3(0001)$, α-$Fe_2O_3(10\bar{1}0)$, and α-$Fe_2O_3(1\bar{2}10)$ facets of clean and hydrogenated surfaces (cf. Sections 2.2.1 and 2.2.2 of the main text). The resulting free-energy landscapes for these reaction pathways are analyzed using the potential-dependent $G_{max}(U)$ descriptor, [37,38] which is defined as the largest free-energy span among the free energies of the reaction intermediates in a free-energy diagram at a given applied electrode potential U [30]:

$$G_{max}(U) = \max\{\Delta G_{span\#k}(U),\ k = 1,\ \ldots,\ m\} \tag{6}$$

A smaller $G_{max}(U)$ therefore corresponds to a smaller thermodynamic bottleneck along the considered reduction sequence and is taken here as an indicator of greater thermodynamic reduction propensity at a given electrode potential. This descriptor enables a consistent comparison of different facets and surface states, provided the reduction sequences comprise the same extent of reduction, without implying an explicit evaluation of activation barriers or reaction kinetics.

Crystallographic dependence of the initial electrochemical reduction

To isolate the intrinsic influence of crystallographic orientation on the initial electrochemical reduction of hematite, we first consider the clean (0001), $(10\bar{1}0)$, and $(1\bar{2}10)$ surfaces as common reference states. Although the AIMD simulations indicate that the nominally clean hematite surface is susceptible to hydroxylation under aqueous conditions, the clean surfaces provide a well-defined reference for disentangling the effect of crystallographic orientation from that of surface hydrogenation.

The equilibrium potential for the reduction of hematite to iron, obtained from data of thermodynamic tables [39] is –0.06 V vs. RHE. To probe the facet dependence under sufficiently reducing conditions, we evaluate hematite reduction at U = –0.7 V vs. RHE. This strongly

cathodic potential was selected to provide a sufficiently large thermodynamic driving force for the initial reduction and to establish a common electrochemical reference for comparing the different crystallographic facets and surface states. **Figure 3** shows the potential-dependent free-energy landscape for the initial reduction of the clean α-Fe_2O_3(0001) surface at U = –0.7 V vs. RHE. The corresponding free-energy diagrams for the clean $(10\bar{1}0)$ and clean $(1\bar{2}10)$ surfaces are provided in **Figures S6** and **S7** of the SI (cf. Section **S6** of the SI). Pronounced differences in the limiting free-energy spans are observed among the three crystallographic orientations. The (0001) facet exhibits a $G_{max}(U = -0.7\ V)$ value of 0.67 eV, compared with 1.02 eV for $(10\bar{1}0)$ and 0.79 eV for $(1\bar{2}10)$. Thus, the (0001) surface displays the smallest thermodynamic bottleneck among the investigated orientations, identifying this facet as intrinsically most favorable for the initial electrochemical reduction under the considered conditions.

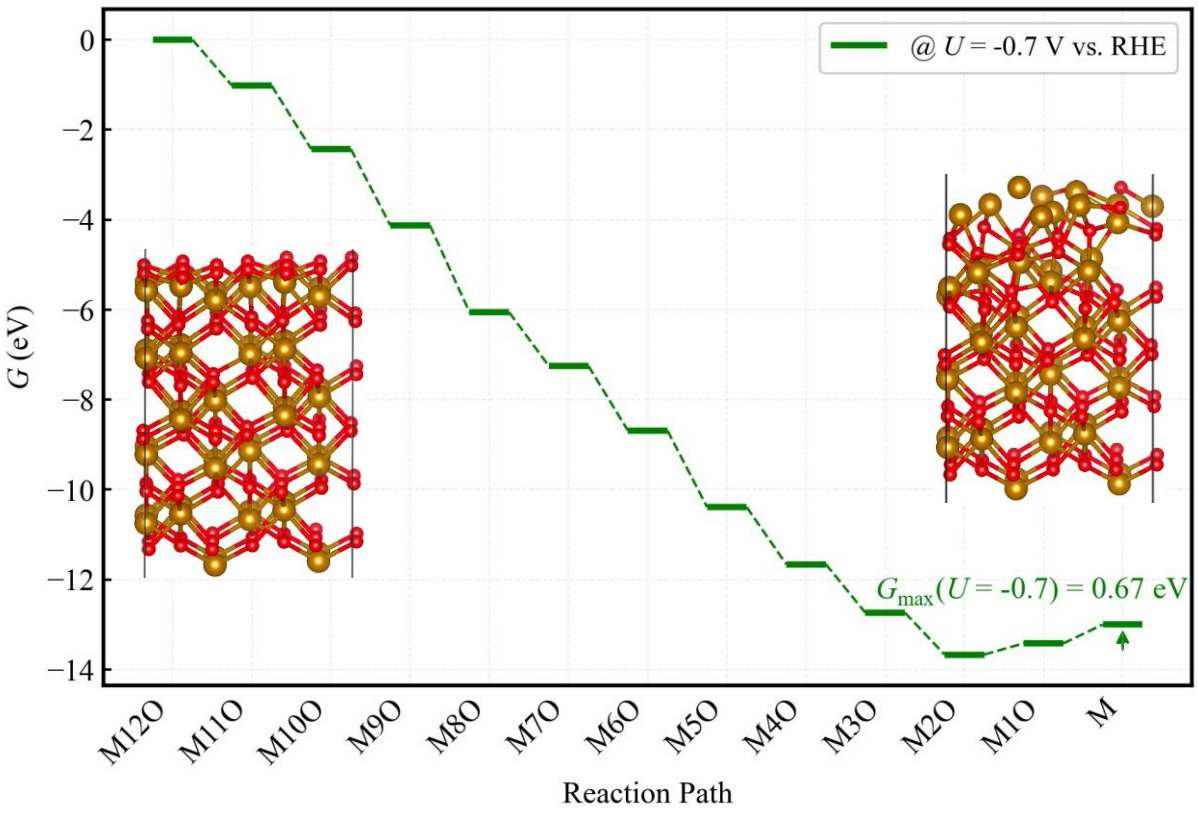


Figure 3. Potential-dependent free-energy diagram for the electrochemical reduction of the α-Fe_2O_3(0001)-clean surface. The green arrow indicates the limiting free-energy span based on the $G_{max}(U)$ descriptor at U = –0.7 V vs. RHE. The inset images on the left and right depict the optimized surface structures before (M−12O) and after reduction (M), respectively. All potential-dependent free-energy diagrams for the electrochemical reduction of the clean α-Fe_2O_3 surfaces for all facets are provided in **Figures S5–S7** of the SI (cf. Section **S6** of the SI).

Crystallographic orientation also affects the position of the limiting free-energy span along the reduction sequence. For the (0001) surface, the largest span corresponds to the late-stage

transformation from M−2O to M. In contrast, the limiting spans of the $(10\bar{1}0)$ and $(1\bar{2}10)$ surfaces refer to the transformations M−4O → M−1O and M−4O → M−2O, respectively. These differences indicate that crystallographic orientation influences not only the magnitude of the thermodynamic bottleneck but also the stage of the initial reduction sequence at which the most unfavorable transformation occurs. All free-energy spans considered for the clean surfaces are listed in **Table S5** (cf. Section **S5** of the SI).

Surface hydrogenation modulates facet-dependent reducibility

Surface hydrogenation can substantially modify the thermodynamics of the initial hematite reduction while preserving the advantage of the (0001) orientation. **Figure 4** summarizes the $G_{max}(U = -0.7\ V)$ values for the clean, 8^*H_{sub}, and 12^*H_{sub} configurations of all three investigated facets; all free-energy spans considered are listed in **Tables S6** and **S7** (cf. Section **S5** of the SI). The clean and 12^*H_{sub} sequences comprise the removal of all twelve oxygen atoms of the near-surface region, whereas the 8^*H_{sub} sequence comprises only the removal of the eight hydroxylated oxygen atoms and thus represents a partial reduction (hatched bars in **Figure 4**). The effect of hydrogenation on the complete reduction is therefore assessed by comparing the clean and 12^*H_{sub} surfaces, whereas the 8^*H_{sub} values are compared only between facets.

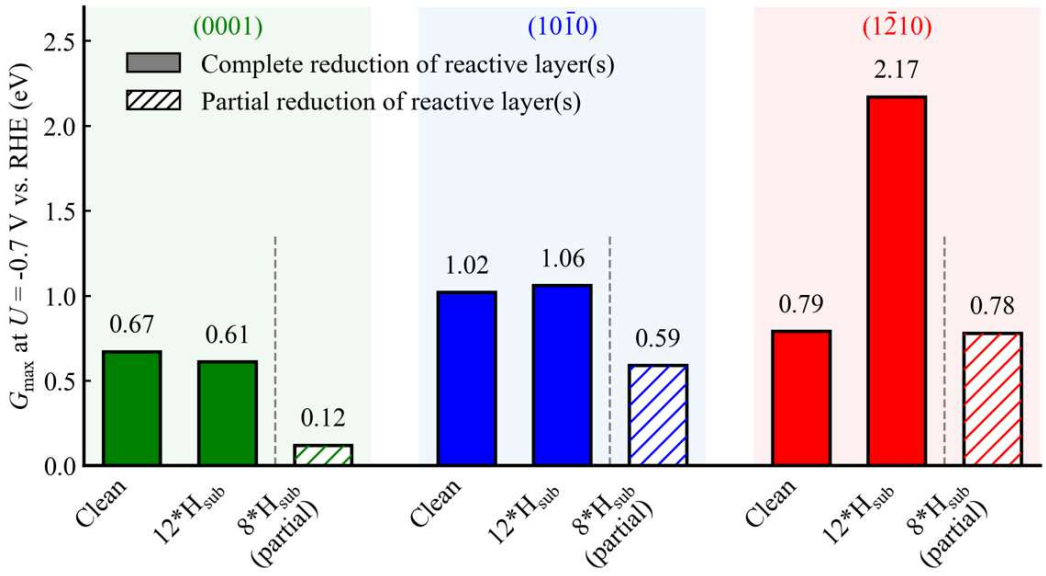


Figure 4. Summary of the $G_{max}(U = -0.7$ V vs. RHE) values for clean, 8^*H_{sub}, and 12^*H_{sub} surface coverages of the (0001), $(10\bar{1}0)$, and $(1\bar{2}10)$ facets of hematite. Color code: green bars represent the (0001) facet, blue bars represent the $(10\bar{1}0)$ facet, and red bars represent the $(1\bar{2}10)$ facet. The hatched bars denote a partial reduction: for 8^*H_{sub}, only the eight hydroxylated oxygen atoms are removed, whereas the clean and 12^*H_{sub} sequences comprise the removal of all twelve oxygen atoms. Surface coverage information is indicated below each bar.

For the complete reduction, high hydrogen coverage affects the three facets in a strikingly different manner. On (0001) and $(10\bar{1}0)$, $G_{max}(U = -0.7\ V)$ remains essentially unchanged upon going from the clean to the 12^*H_{sub} surface (0.67 vs. 0.61 eV and 1.02 vs. 1.06 eV, respectively). On $(1\bar{2}10)$, in contrast, $G_{max}(U = -0.7\ V)$ increases from 0.79 to 2.17 eV so that the highly hydrogenated surface is considerably more difficult to reduce. Since 12^*H_{sub} corresponds to the thermodynamically preferred hydrogen coverage under the considered conditions, the most stable interfacial state is not necessarily the most reducible one: high hydrogen coverage can passivate the surface toward further reduction, and the extent of this passivation depends strongly on the crystallographic orientation.

For the partial reduction of the 8^*H_{sub} surfaces, $G_{max}(U = -0.7\ V)$ amounts to 0.12 eV for (0001), 0.59 eV for $(10\bar{1}0)$ and 0.78 eV for $(1\bar{2}10)$. These smaller values do not indicate a facilitated reduction: for the complete clean and 12^*H_{sub} sequences, the limiting spans arise in the late stage of the reduction (cf. **Figure 3** and **Figures S12**, **S16**, and **S19** in Section **S6.2** of the SI), which the partial sequence does not include.

Importantly, the (0001) facet retains the lowest $G_{max}(U = -0.7\ V)$ for every investigated surface state, including the partial reduction of 8^*H_{sub}. The enhanced reducibility of (0001) is therefore robust against substantial changes in the interfacial hydrogen coverage, whereas the relative behavior of the two non-basal facets is more strongly coverage-dependent. These findings identify crystallographic orientation and surface hydrogenation as coupled but distinct factors governing the initial electrochemical reduction of hematite.

Although hydrogenation is not thermodynamically favorable on the outermost Fe sites compared to the oxygen surface sites, we also investigated hematite reduction as a function of hydrogen atoms adsorbed on the outermost Fe atoms on the (0001), $(10\bar{1}0)$, and $(1\bar{2}10)$ facets. This is motivated by the possibility that the Fe-surface sites may play a role in the early stages of reduction, despite their lower thermodynamic preference. The trend observed in **Figure 4** for hydrogenated $^*H_{sub}$ states also holds for a monolayer of hydrogen atoms adsorbed on the outermost Fe atoms (cf. **Figure 5a**), as the (0001) facet still exhibits the highest reduction propensity.

Based on this result, we further examined the impact of hydrogen atoms adsorbed on the outermost Fe atoms (*H) in combination with the 12^*H_{sub} state for the (0001) facet. Note that for the $(10\bar{1}0)$, and $(1\bar{2}10)$ facets, such coverages were found to be thermodynamically unstable due to water formation on the surface.

For the complete reduction sequences, additional hydrogenation of the lattice oxygen raises $G_{max}(U = -0.7\ V)$ from 0.00 eV (4*H & clean) to 0.44 eV (4*H & 12*H_{sub}) (**Figure 5b**). Hydrogen adsorbed on both the outermost Fe atoms and the lattice oxygen therefore hinders the reduction of (0001).

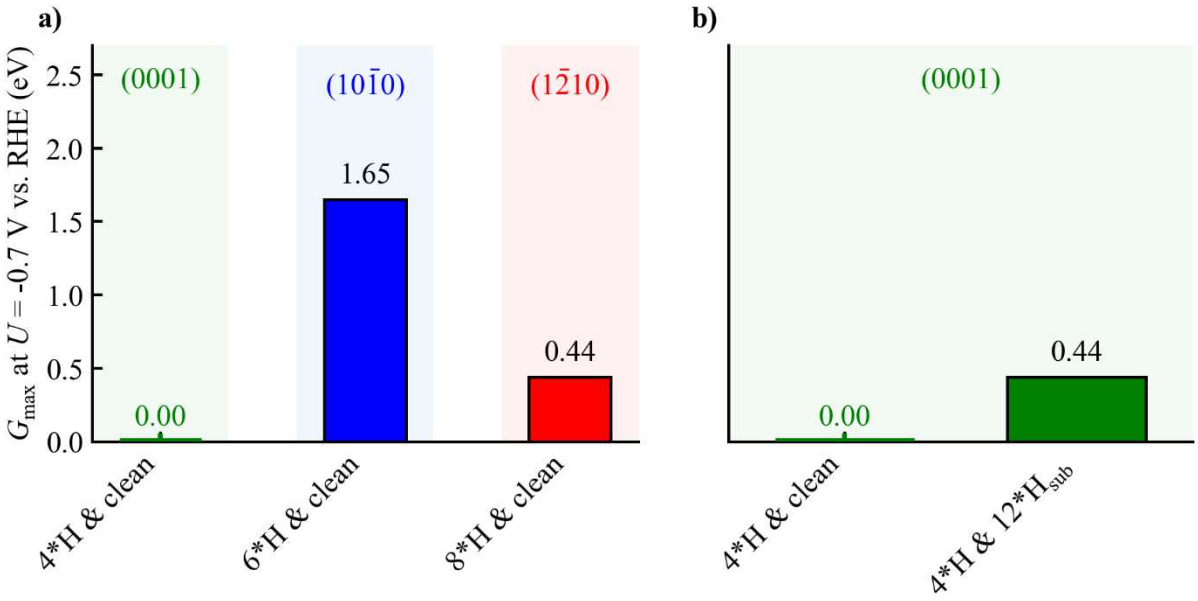


Figure 5. Summary of the $G_{max}(U = -0.7$ V vs. RHE) values for **a)** 4*H & clean(0001), 6*H & clean(10$\bar{1}$0), and 8*H & clean(1$\bar{2}$10) surface coverages of hematite and **b)** 4*H & clean (0001) and 4*H & 12*H_{sub}(0001) surface coverages of hematite. Color code: green bars represent the (0001) facet, blue bars represent the (10$\bar{1}$0) facet, and red bars represent the (1$\bar{2}$10) facet. Surface coverage information is indicated below each bar.

Detailed potential-dependent free-energy diagrams for the hydrogenated surfaces (*H_{sub} states), as a function of hydrogen adsorption on the outermost Fe sites (*H states), and comparisons with gas-phase DFT calculations, are provided in **Figures S8–S19** (cf. Section **S6** of the SI).

Electronic-structure changes upon reduction

Having established the effects of crystallographic orientation and surface hydrogenation on the thermodynamics of the initial hematite reduction, we next examine how the electronic structure evolves during the reduction and whether band-center descriptors can rationalize these trends. To this end, the Fe d-band and O p-band centers were evaluated for the investigated facets and surface coverages before and after reduction. The corresponding values for the reactive and non-reactive atomic layers, as well as for the complete surface models, are provided in **Tables S8–S12** of the SI (cf. Section **S7** of the SI).

The Fe d-band center does not exhibit a systematic relationship with the calculated $G_{max}(U = -0.7\ V)$ values (cf. **Figures S20–S22** in Section **S7** of the SI). In contrast, the O p-band center, evaluated for the non-reactive oxygen layers because only these oxygen atoms are present both before and after reduction, reveals a distinct electronic response of the (0001) facet. Upon reduction, it shifts to more negative energies for most surface states, and this downward shift is largest on (0001), both on average over the complete reduction sequences (–0.53 eV, compared with –0.34 eV for $(10\bar{1}0)$ and –0.16 eV for $(1\bar{2}10)$) and for both hydrogen-covered states (–0.55 eV and –0.64 eV for 4*H and 12*H_{sub}, respectively), whereas the shifts on the clean surfaces are comparable for all facets (**Figure 6**). This pronounced electronic response qualitatively parallels the highest reducibility of the (0001) facet. However, the O p-band center does not reproduce the ordering of the two non-basal facets, and neither its shift nor its initial value correlates systematically with $G_{max}(U = -0.7\ V)$ across the complete sequences. It thus serves as a qualitative indicator of the strong electronic response of the (0001) facet rather than as a quantitative descriptor of reducibility.

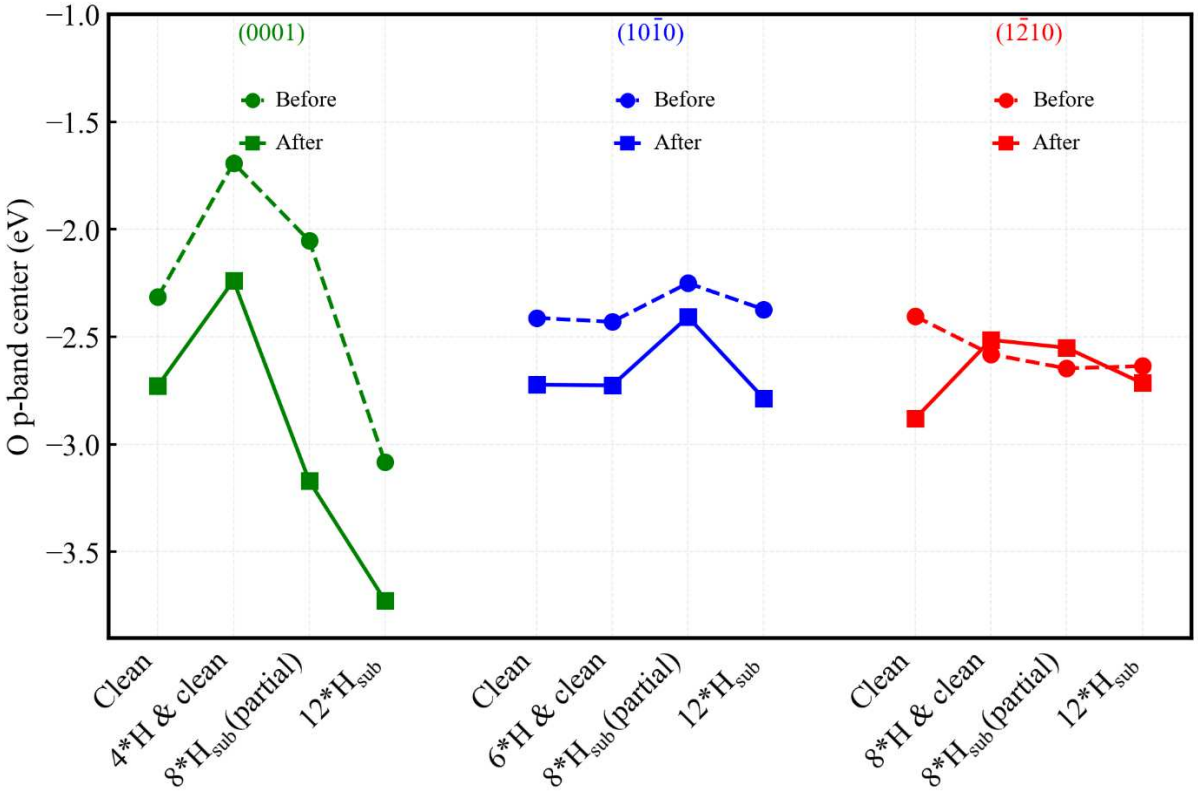


Figure 6. O p-band center of the non-reactive oxygen layers before (circles, dashed lines) and after (squares, solid lines) the electrochemical reduction for the investigated surface states of the (0001), $(10\bar{1}0)$, and $(1\bar{2}10)$ facets (green, blue, and red, respectively), evaluated within the energy interval of –10 to 4 eV. The 8*H_{sub} values refer to the partial reduction and are not included in the facet-averaged shifts discussed in the text. Lines are guides to the eye. The corresponding values are listed in **Table S11** of the SI.

Finally, we analyzed the density of states (DOS) for the investigated facets and surface coverages before and after reduction. Prior to reduction, the electronic structure near the valence and conduction bands are predominantly influenced by O p-states. After reduction, however, Fe d-states become the dominant contributors in these energy regions, as shown in **Figure 7** for the reduction of the clean (0001) surface. The emergence of Fe d-derived states near the Fermi level indicates a transition toward more metallic electronic character during the initial electrochemical reduction of hematite, suggesting the formation of a reduced, Fe-rich surface phase.

Similar trends were observed across the other facets, with corresponding DOS plots provided in **Figures S25-S33** in the SI (cf. Section **S8** of the SI). For most cases, the band gap decreases upon reduction, suggesting a transition toward a more metallic character compared with the unreduced surfaces.

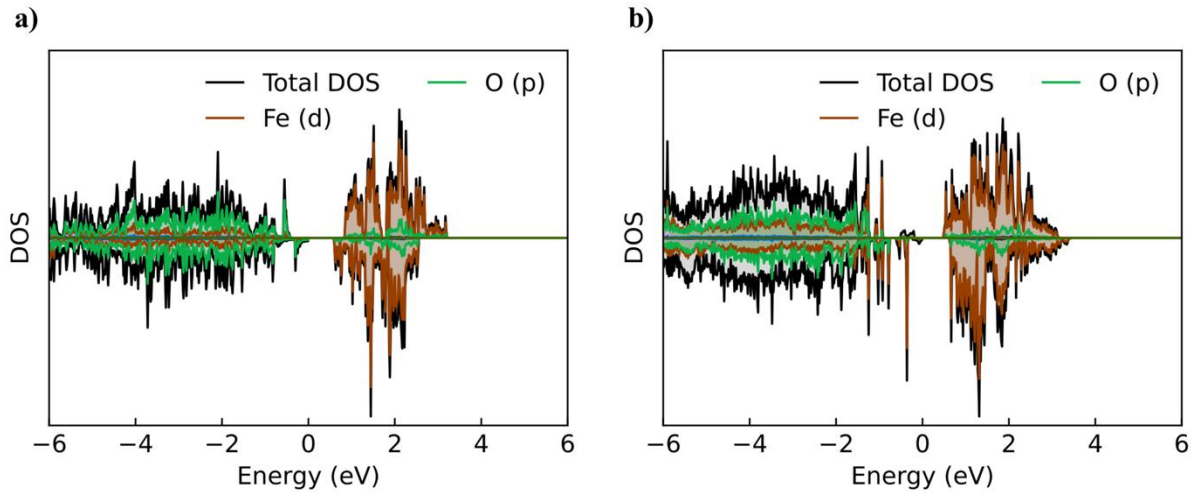


Figure 7. DOS of α-Fe_2O_3(0001)-clean surface. **a)** Before electrochemical reduction, and **b)** after electrochemical reduction.

Fe nucleation from dissolved Fe^{2+} and Fe^{3+} on reduced hematite surfaces

To assess whether a dissolution–deposition pathway competes with the direct solid-state reduction, we evaluate the deposition of one and two Fe atoms from dissolved Fe^{2+} or Fe^{3+} onto the reduced surfaces (cf. Section **S10** of the SI). The Fe^{2+}/ Fe^{3+} reference is derived from the experimental standard potential at pH = 0 and unit activity, together with the computed chemical potential of bulk bcc Fe.

At U = –0.7 V, the deposition of bulk Fe is exergonic by 0.50 eV per Fe atom from Fe^{2+} and by 1.98 eV from Fe^{3+} (cf. Section **S10** of the SI). In contrast, the deposition of isolated Fe

adatoms onto the reduced surfaces is endergonic for all investigated facets and surface states, by at least 2.1 eV from Fe^{2+} and 0.6 eV from Fe^{3+} (**Table S14**), because a single Fe adatom is 2.6–5.0 eV less stable than an Fe atom in bulk bcc iron.

These results do not exclude Fe electrodeposition as such, which becomes thermodynamically favorable once a bulk-like Fe phase is present. Rather, they show that the nucleation of Fe from dissolved species on the reduced hematite surfaces faces a substantial thermodynamic barrier, whereas the solid-state pathway generates reduced Fe directly within the existing Fe–O framework. This supports the relevance of the solid-state pathway for the initial reduction stage, in line with recent experimental findings,[28] while dissolution–deposition may contribute once Fe nuclei have formed, consistent with the proposed coexistence of both mechanisms.[21,25] Since the analysis refers to pH = 0 and unit activity of Fe^{2+}/ Fe^{3+}, it does not directly address alkaline electrolytes, in which dissolved iron is present as hydroxo complexes at low concentrations.

Discussion

The combined thermodynamic and electronic-structure analysis indicates that the initial electrochemical reduction of hematite is governed by an interplay between crystallographic orientation and the evolving chemical state of the surface. Surface hydrogenation modifies the accessibility of individual reduction steps, yet the (0001) facet consistently remains the most favorable orientation. This persistence suggests that the enhanced reducibility of (0001) is not solely associated with a particular surface coverage but reflects an intrinsic crystallographic contribution to the reduction process.

At the same time, surface hydrogenation does not substantially promote the complete reduction. The highly hydrogenated 12^*H_{sub} state, which is thermodynamically preferred under the considered conditions, leaves the reduction thermodynamics of (0001) and $(10\bar{1}0)$ essentially unchanged but strongly impedes the reduction of $(1\bar{2}10)$. The thermodynamically most stable interfacial state is therefore not necessarily the most reducible one, and the extent of this passivation depends on the crystallographic orientation. The reduction propensity of hematite is thus determined not only by the crystallographic structure of the oxide but also by the evolution of its interfacial chemical state.

The predicted crystallographic preference is particularly noteworthy in light of experimentally observed anisotropy during hydrogen-based reduction of hematite. Ratzker *et al*. investigated hematite samples at the single-crystal level with the same crystallographic orientations considered here and identified the (0001) orientation as the most readily reduced one, using molecular hydrogen as a feedstock.[9] Additional experimental and computational study has likewise demonstrated pronounced facet effects during hydrogen reduction of hematite at solid–gas interfaces.[29] The agreement in crystallographic sensitivity across these studies and the present calculations in an electrochemical environment suggests that part of the experimentally observed anisotropy originates from intrinsic differences in the reducibility of the hematite lattice.

This correspondence should not be interpreted as evidence that electrochemical and hydrogen-based reduction proceed through identical elementary mechanisms. Hydrogen-based reduction involves a gas–solid reaction environment and, at later stages, phase-boundary migration and structural evolution through progressively reduced iron oxides. [6–9,11] In contrast, the present model isolates the initial, surface-localized proton-coupled electron transfer steps under electrochemical conditions. The persistence of crystallographic anisotropy across these distinct reaction environments nevertheless suggests that the local Fe–O bonding of the exposed hematite facets, reflected in their distinct electronic response upon reduction, exerts a fundamental influence on the earliest stages of reduction.

While crystallographic orientation provides an intrinsic contribution to hematite reducibility, surface hydrogenation modulates how this intrinsic tendency is expressed under electrochemical conditions. This interplay may offer a route toward controlling the early stages of electrochemical iron-oxide reduction through the crystallographic and interfacial properties of the starting material. For instance, hematite particles with a high fraction of exposed (0001) surfaces, such as platelets, should be reduced more readily, whereas morphologies dominated by $(1\bar{2}10)$ surfaces are prone to passivation at high hydrogen coverage.

Under the strongly cathodic conditions considered here, the reduction of hematite competes with the hydrogen evolution reaction (HER), which limits the current efficiency of electrochemical iron production.[18] Preliminary calculations of hydrogen adsorption on surface Fe sites indicate that this competition intensifies as the reduction proceeds: the hydrogen adsorption free energy, which governs the thermodynamics of the Volmer–Heyrovsky mechanism, amounts to roughly 0.5 eV on the hydrogenated surfaces at $U = 0$ V vs. RHE but

approaches 0 eV on the reduced surfaces. The HER is therefore thermodynamically facile on both surface states at $U = -0.7$ V vs. RHE, so that the selectivity toward iron formation is likely governed by kinetic factors beyond the present thermodynamic analysis.

In summary, we investigated the initial electrochemical reduction of hematite on the $(0001), (10\bar{1}0)$, and $(1\bar{2}10)$ facets using DFT + U calculations combined with potential-dependent free-energy analysis, electronic-structure analysis, and AIMD simulations. The calculated reduction pathways reveal a pronounced crystallographic dependence, with the (0001) facet consistently exhibiting the smallest $G_{max}(U = -0.7\ \text{V})$ value and thus the highest thermodynamic reduction propensity among the investigated orientations.

Upon reduction, Fe d-derived states emerge near the Fermi level, indicating the formation of a more metallic, Fe-rich surface. The O p-band center shifts most strongly on the (0001) facet, which qualitatively parallels its highest reducibility, whereas neither the O p-band nor the Fe d-band center provides a quantitative descriptor of the facet ranking.

Finally, the deposition of isolated Fe adatoms from dissolved Fe^{2+} or Fe^{3+} onto the reduced surfaces is strongly endergonic, although bulk Fe deposition is exergonic at the investigated potential. Nucleation from solution is therefore thermodynamically hindered on these surfaces, which supports the relevance of the direct solid-state pathway for the initial reduction stage. Overall, the present study establishes crystallographic orientation and interfacial hydrogenation as key factors governing the initial electrochemical reduction of hematite and provides an atomistic basis for understanding and potentially controlling facet-dependent reducibility in electrochemical iron production.

Methods

DFT calculations. To investigate the initial electrochemical reduction of hematite (α-Fe_2O_3) on the $(0001), (10\bar{1}0)$, and $(1\bar{2}10)$ facets under varying surface coverages, we performed density functional theory (DFT) using the Vienna *Ab initio* Simulation Package (VASP) [40–42]. The aqueous environment was represented using the implicit-solvation model VASPsol. [43] The projector augmented wave (PAW) method [44] was used to describe core-valence electron interactions, with 14 and 6 valence electrons assigned to Fe and O, respectively. All calculations were carried out within the spin-polarized plane-wave DFT framework using Perdew-Burke-Ernzerhof (PBE) functional [45], supplemented with an on-site Coulomb

interaction (PBE + U). [46] The effective U value for the 3d states is typically set between 4.0 and 4.3 eV [47–49], and in this study we adopt U = 4.2 eV, which yields a band gap of 2.14 eV—consistent with previous experimental and computational findings.[47,48,50–55] Grimme's D3 dispersion correction [56] was included to account for a long-range van der Waals interactions, improving the accuracy of surface and adsorption energetics. To minimize interactions between periodic images, a vacuum layer of at least 16 Å was introduced along the surface-normal (z) direction. Given the use of an asymmetric slab model, a dipole correction was applied perpendicular to the surface to mitigate artificial electrostatic interactions.[57]

***Ab initio* molecular dynamics**. To assess the finite-temperature stability of representative surface configurations of hematite in an explicit aqueous environment, we performed AIMD simulations using the CP2K 2025.2 [58]/Quickstep software package [59], which implements a hybrid Gaussian and plane-wave (GPW) approach. A Hubbard effective U value of 3.2 eV was employed for Fe states in the CP2K calculations, yielding a band gap of 2.06 eV, consistent with the electronic structure obtained using the VASP setup. Within this framework, the Kohn–Sham orbitals were expanded in atom-centered Gaussian-type basis sets, while the electronic density is represented on an auxiliary plane-wave grid.[60] Core-electron effects are accounted for using analytical Goedecker–Teter–Hutter (GTH) pseudopotentials.[61,62] The Fe and O atoms were described using double-ζ basis with polarization functions, specifically the DZVP-MOLOPT-SR-GTH basis sets [63], while H was described using the DZVP-MOLOPT-GTH basis set.[63] The basis functions were taken from the BASIS_MOLOPT library.[63] The plane-wave cutoff for the electronic density was set to 600 Ry, with a relative multigrid cutoff of 60 Ry. Further computational details are given in section **S1** of the Supporting Information (SI).

Data availability

The optimized structures and the input and output files of all DFT and AIMD calculations supporting the findings of this study will be deposited upon publication in a public repository. All other data are available within the article and its Supplementary Information.

Code availability

DFT calculations were performed with the commercial code VASP, and AIMD simulations with the open-source code CP2K. The free-energy diagrams were analyzed with the $G_{max}(U)$ descriptor following refs. [37] and [38].

References

1. Fan, Z. & Friedmann, S. J. Low-carbon production of iron and steel: Technology options, economic assessment, and policy. *Joule* **5**, 829–862 (2021).

2. Bergthorson, J. M. Recyclable metal fuels for clean and compact zero-carbon power. *Prog. Energy Combust. Sci.* **68**, 169–196 (2018).

3. Kim, J. *et al.* Decarbonizing the iron and steel industry: A systematic review of sociotechnical systems, technological innovations, and policy options. *Energy Res. Soc. Sci.* **89**, 102565 (2022).

4. Spreitzer, D. & Schenk, J. Reduction of Iron Oxides with Hydrogen—A Review. *Steel Res. Int.* **90**, 1900108 (2019).

5. Rukini, A., Rhamdhani, M. A., Brooks, G. A. & Van den Bulck, A. Metals Production and Metal Oxides Reduction Using Hydrogen: A Review. *J. Sustain. Metall.* **8**, 1–24 (2022).

6. Hammam, A. *et al.* Studies on the Reduction Behavior of Iron Oxide Pellet Fines with Hydrogen Gas: Mechanism and Kinetic Analysis. *J. Sustain. Metall.* **9**, 1289–1302 (2023).

7. Özgün, Ö., Dirba, I., Gutfleisch, O., Ma, Y. & Raabe, D. Green Ironmaking at Higher H2 Pressure: Reduction Kinetics and Microstructure Formation During Hydrogen-Based Direct Reduction of Hematite Pellets. *J. Sustain. Metall.* **10**, 1127–1140 (2024).

8. Heidari, A., Niknahad, N., Iljana, M. & Fabritius, T. A review on the kinetics of iron ore reduction by hydrogen. *Materials* **14**, 7540 (2021).

9. Ratzker, B., Ruffino, M., Shankar, S., Raabe, D. & Ma, Y. Elucidating the microstructure evolution during hydrogen-based direct reduction via a case study of single crystal hematite. *Acta Mater.* **294**, 121174 (2025).

10. Ma, Y. *et al.* Reducing Iron Oxide with Ammonia: A Sustainable Path to Green Steel. *Adv. Sci.* **10**, 2300111 (2023).

11. Ma, Y. *et al.* Hierarchical nature of hydrogen-based direct reduction of iron oxides. *Scr. Mater.* **213**, 114571 (2022).

12. Shahabuddin, M., Brooks, G. & Rhamdhani, M. A. Decarbonisation and hydrogen integration of steel industries: Recent development, challenges and technoeconomic analysis. *J. Clean. Prod.* **395**, 136391 (2023).

13. Wiencke, J., Lavelaine, H., Panteix, P. J., Petitjean, C. & Rapin, C. Electrolysis of iron in a molten oxide electrolyte. *J. Appl. Electrochem.* **48**, 115–126 (2018).

14. Allanore, A. Features and Challenges of Molten Oxide Electrolytes for Metal Extraction. *J. Electrochem. Soc.* **162**, E13–E22 (2015).

15. Allanore, A., Lavelaine, H., Valentin, G., Birat, J. P. & Lapicque, F. Electrodeposition of Metal Iron from Dissolved Species in Alkaline Media. *J. Electrochem. Soc.* **154**, E187 (2007).

16. Feynerol, V., Lavelaine, H., Marlier, P., Pons, M. N. & Lapicque, F. Reactivity of suspended iron oxide particles in low temperature alkaline electrolysis. *J. Appl. Electrochem.* **47**, 1339–1350 (2017).

17. Allanore, A., Lavelaine, H., Birat, J. P., Valentin, G. & Lapicque, F. Experimental investigation of cell design for the electrolysis of iron oxide suspensions in alkaline electrolyte. *J. Appl. Electrochem.* **40**, 1957–1966 (2010).

18. Majid, A. I. *et al.* Comparative study of electroreduction of iron oxide using acidic and alkaline electrolytes for sustainable iron production. *Electrochim. Acta* **467**, 142942 (2023).

19. Díaz, S. L., Calderón, J. A., Barcia, O. E. & Mattos, O. R. Electrodeposition of iron in sulphate solutions. *Electrochim. Acta* **53**, 7426–7435 (2008).

20. Su, C., He, F., Ju, H., Zhang, Y. & Wang, E. Electrodeposition of Ni, Fe and Ni-Fe alloys on a 316 stainless steel surface in a fluorborate bath. *Electrochim. Acta* **54**, 6257–6263 (2009).

21. Majid, A. I., Finotello, G., van der Schaaf, J., Deen, N. G. & Tang, Y. On the formation of dendritic iron from alkaline electrochemical reduction of iron oxide prepared for metal fuel applications. *Chem. Eng. Sci.* **291**, 119931 (2024).

22. Ishikawa, K., Yoshioka, T., Sato, T. & Okuwaki, A. Solubility of hematite in LiOH, NaOH and KOH solutions. *Hydrometallurgy* **45**, 129–135 (1997).

23. Lausch, M., Brockmann, P., Schmitt, F., Etzold, B. J. M. & Hussong, J. In-situ iron oxide particle size and shape evolution during the dissolution in oxalic acid. *Chem. Eng. Sci.* **289**, 119864 (2024).

24. Vehmaanperä, P., Salmimies, R. & Häkkinen, A. Thermodynamic and Kinetic Studies of Dissolution of Hematite in Mixtures of Oxalic and Sulfuric Acid. *Min. Metall. Explor.* **38**, 69–80 (2021).

25. Lopes, D. V., Quina, M. J., Frade, J. R. & Kovalevsky, A. V. Prospects and challenges of the electrochemical reduction of iron oxides in alkaline media for steel production. *Front. Mater.* **9**, 1010156 (2022).

26. Qi, J. *et al.* Porous Nickel–Iron Oxide as a Highly Efficient Electrocatalyst for Oxygen Evolution Reaction. *Adv. Sci.* **2**, 1500199 (2015).

27. Zou, X. *et al.* Electroreduction of Iron(III) Oxide Pellets to Iron in Alkaline Media: A Typical Shrinking-Core Reaction Process. *Metallurgical and Materials Transactions B: Process Metallurgy and Materials Processing Science* **46**, 1262–1274 (2015).

28. Méndez Florido, F., Brodersen, A. & Linkhorst, J. Direct electrochemical reduction of iron oxide for metal energy storage - a microfluidic study on the impact of cell design for slurry electrolysis. *Fuel* **415**, 138291 (2026).

29. Han, Y. *et al.* Crystal facet-dependent reduction behavior of α-Fe2O3 in hydrogen atmosphere. *Appl. Surf. Sci.* **638**, 158056 (2023).

30. Kozuch, S. & Shaik, S. How to conceptualize catalytic cycles? the energetic Span model. *Acc. Chem. Res.* **44**, 101–110 (2011).

31. Hansen, H. A., Rossmeisl, J. & Nørskov, J. K. Surface Pourbaix diagrams and oxygen reduction activity of Pt, Ag and Ni(111) surfaces studied by DFT. *Phys. Chem. Chem. Phys.* **10**, 3722–3730 (2008).

32. Groß, A. Grand-canonical approaches to understand structures and processes at electrochemical interfaces from an atomistic perspective. *Curr. Opin. Electrochem.* **27**, 100684 (2021).

33. Wang, Z., Guo, X., Montoya, J. & Nørskov, J. K. Predicting aqueous stability of solid with computed Pourbaix diagram using SCAN functional. *NPJ Comput. Mater.* **6**, 160 (2020).

34. Sokolov, M. & Exner, K. S. Unraveling the role of Fe and Ni in oxygen evolution reaction on pentlandite using three generations of computational surface models. *NPJ Comput. Mater.* **12**, 61 (2026).

35. Souvi, S. M. O., Badawi, M., Paul, J. F., Cristol, S. & Cantrel, L. A DFT study of the hematite surface state in the presence of H2, H2O and O2. *Surf. Sci.* **610**, 7–15 (2013).

36. Nørskov, J. K. *et al.* Origin of the overpotential for oxygen reduction at a fuel-cell cathode. *J. Phys. Chem. B* **108**, 17886–17892 (2004).

37. Exner, K. S. A universal descriptor for the screening of electrode materials for multiple-electron processes: Beyond the thermodynamic overpotential. *ACS Catal.* **10**, 12607–12617 (2020).

38. Razzaq, S. & Exner, K. S. Materials Screening by the Descriptor Gmax(η): The Free-Energy Span Model in Electrocatalysis. *ACS Catal.* **13**, 1740–1758 (2023).

39. Chase, M. W. , Jr. *NIST-JANAF Thermochemical Tables*. (American Chemical Society and American Institute of Physics for the National Institute of Standards and Technology, 1998).

40. Kresse, G. & Hafner, J. Ab initio molecular dynamics for liquid metals. *Phys. Rev. B Condens. Matter* **47**, 558–561 (1993).

41. Kresse, G. & Furthmüller, J. Efficiency of ab-initio total energy calculations for metals and semiconductors using a plane-wave basis set. *Comput. Mater. Sci.* **6**, 15–50 (1996).

42. Kresse, G. & Furthmüller, J. Efficient iterative schemes for ab initio total-energy calculations using a plane-wave basis set. *Phys. Rev. B Condens. Matter Mater. Phys.* **54**, 11169–11186 (1996).

43. Mathew, K., Sundararaman, R., Letchworth-Weaver, K., Arias, T. A. & Hennig, R. G. Implicit solvation model for density-functional study of nanocrystal surfaces and reaction pathways. *J. Chem. Phys.* **140**, 084106 (2014).

44. Kresse, G. & Joubert, D. From ultrasoft pseudopotentials to the projector augmented-wave method. *Phys. Rev. B* **59**, 1758 (1999).

45. Perdew, J. P., Burke, K. & Ernzerhof, M. Generalized Gradient Approximation Made Simple. *Phys. Rev. Lett.* **77**, 3865 (1996).

46. Cococcioni, M. & De Gironcoli, S. Linear response approach to the calculation of the effective interaction parameters in the LDA+U method. *Phys. Rev. B Condens. Matter Mater. Phys.* **71**, 035105 (2005).

47. Kiejna, A. & Pabisiak, T. Surface properties of clean and Au or Pd covered hematite (α-Fe2O3) (0001). *J. Phys.: Condens. Matter* **24**, 095003 (2012).

48. Liao, P. & Carter, E. A. Testing variations of the GW approximation on strongly correlated transition metal oxides: hematite (α-Fe2O3) as a benchmark. *Phys. Chem. Chem. Phys.* **13**, 15189–15199 (2011).

49. Toroker, M. C. Theoretical insights into the mechanism of water oxidation on nonstoichiometric and titanium-doped Fe2O3(0001). *J. Phys. Chem. C* **118**, 23162–23167 (2014).

50. Yatom, N., Neufeld, O. & Caspary Toroker, M. Toward Settling the Debate on the Role of Fe2O3 Surface States for Water Splitting. *J. Phys. Chem. C* **119**, 24789–24795 (2015).

51. Ulman, K., Nguyen, M. T., Seriani, N., Piccinin, S. & Gebauer, R. A Unified Picture of Water Oxidation on Bare and Gallium Oxide-Covered Hematite from Density Functional Theory. *ACS Catal.* **7**, 1793–1804 (2017).

52. Nguyen, M. T., Seriani, N., Piccinin, S. & Gebauer, R. Photo-driven oxidation of water on α-Fe2O3 surfaces: An ab initio study. *J. Chem. Phys.* **140**, 064703 (2014).

53. Awulachew, S. S., Dhaka, K., Tayyebi, E. & Exner, K. S. Atomic-scale insights into the oxygen evolution reaction on hematite: a detailed mechanistic investigation of different surface coverages. *J. Mater. Chem. A Mater.* **13**, 36104 (2025).

54. Cheng, C., Zhu, Y., Zhou, Z., Long, R. & Fang, W. H. Photoinduced small electron polarons generation and recombination in hematite. *NPJ Comput. Mater.* **8**, 148 (2022).

55. Chen, H., Bienvenu, B., Todorova, M., Freysoldt, C. & Neugebauer, J. Universal alignment of defect thermodynamics in hematite. *NPJ Comput. Mater.* **12**, 284 (2026).

56. Grimme, S., Antony, J., Ehrlich, S. & Krieg, H. A consistent and accurate ab initio parametrization of density functional dispersion correction (DFT-D) for the 94 elements H-Pu. *J. Chem. Phys.* **132**, 154104 (2010).

57. Bengtsson, L. Dipole correction for surface supercell calculations. *Phys. Rev. B* **59**, 12301–12304 (1999).

58. Kühne, T. D. *et al.* CP2K: An electronic structure and molecular dynamics software package -Quickstep: Efficient and accurate electronic structure calculations. *J. Chem. Phys.* **152**, 194103 (2020).

59. Vandevondele, J. *et al.* Quickstep: Fast and accurate density functional calculations using a mixed Gaussian and plane waves approach. *Comput. Phys. Commun.* **167**, 103–128 (2005).

60. Lippert, G., Hutter, J. & Parrinello, M. A hybrid Gaussian and plane wave density functional scheme. *Mol. Phys.* **92**, 477–488 (1997).

61. Goedecker, S. & Teter, M. Separable dual-space Gaussian pseudopotentials. *Phys. Rev. B* **54**, 1703 (1996).

62. Hartwigsen, C., Goedecker, S. & Hutter, J. Relativistic separable dual-space Gaussian pseudopotentials from H to Rn. *Phys. Rev. B* **58**, 3641 (1998).

63. VandeVondele, J. & Hutter, J. Gaussian basis sets for accurate calculations on molecular systems in gas and condensed phases. *J. Chem. Phys.* **127**, 114105 (2007).

Competing interests

The authors declare no competing interests.

Author contributions

K.S.E. conceived the study. S.S.A. performed the calculations, analyzed the data, prepared the figures, and wrote the original draft. K.S.E. supervised the project, provided resources, acquired funding, and revised the manuscript. Both authors discussed the results and edited the manuscript.

Acknowledgments

SSA acknowledges the German Academic Exchange Service (DAAD) scholarship and International Max Planck Research School for Sustainable Metallurgy (IMPRS SusMet) for the financial support to carry out this study. SSA also gratefully acknowledges Dr. Ebrahim Tayyebi for the fruitful discussions and valuable scientific insights that contributed to this work. SSA further acknowledges Dr. David Hernández-Castillo for his assistance in designing the figures for this publication. KSE further acknowledges funding by the Deutsche Forschungsgemeinschaft through the RESOLV Cluster of Excellence (EXC 2033 – 390677874 – RESOLV). The authors gratefully acknowledge the computing time granted by the Center for Computational Sciences and Simulation (CCSS) of the Universität of Duisburg-Essen and

provided on the supercomputer amplitUDE (DFG project 459398823; grant ID INST 20876/423-1 FUGG) at the Zentrum für Informations- und Mediendienste (ZIM).

Supplementary Files

This is a list of supplementary files associated with this preprint. Click to download.

- AwulachewFe2O3ReductionSIFINAL.pdf